On CSI-Based Vital Sign Monitoring Using Commodity WiFi

XUYU WANG, California State University
CHAO YANG and SHIWEN MAO, Auburn University

Vital signs, such as respiration and heartbeat, are useful for health monitoring because such signals provide important clues of medical conditions. Effective solutions are needed to provide contact-free, easy deployment, low-cost, and long-term vital sign monitoring. In this article, we present PhaseBeat to exploit channel state information, in particular, phase difference data to monitor breathing and heart rates with commodity WiFi devices. We provide a rigorous analysis of channel state information phase difference with respect to its stability and periodicity. Based on the analysis, we design and implement the PhaseBeat system with off-the-shelf WiFi devices and conduct an extensive experimental study to validate its performance. Our experimental results demonstrate the superior performance of PhaseBeat over existing approaches in various indoor environments.

CCS Concepts: • **Applied computing → Health informatics**; • **Human-centered computing → Mobile devices**;

Additional Key Words and Phrases: Channel state information, commodity 5-GHz WiFi, health sensing, vital sign monitoring

1 INTRODUCTION

It is estimated that more than 100 million Americans have chronic health conditions, such as lung disorder and heart diseases, and three fourths of the total U.S. healthcare cost is spent treating these diseases [Boric-Lubeke and Lubecke 2002]. There is an increasing demand for long-term health monitoring in indoor environments to reduce healthcare cost. Vital signs, such as respiration and heartbeat, are useful to physical health monitoring because such signals can provide important clues to medical problems, such as sleep disorder or anomalies (e.g., apnea) and sudden infant death syndrome (SIDS) [Hunt and Hauck 2006]. Most traditional methods for vital sign monitoring require a person to wear special devices such as a capnometer [Mogue and Rantala 1988] or a pulse oximeter [Shariati and Zahedi 2005]. Such technologies are inconvenient to use and uncomfortable for the

patient. Alternative solutions of contact-free, easy deployment, low-cost, and long-term vital sign monitoring would be highly appealing.

Various forms of contact-free sensors have been proposed to detect human vital signs, such as cameras, smartphones, and geophones. Camera-based techniques can monitor the breathing rate and heart rate by analyzing the captured video of human body [Scully et al. 2010]. However, the system requires sufficient surrounding light to achieve the best performance. Thus, it may not be suitable for sleep monitoring. To address the influence of a dark sensing environment, acoustic signals are proposed for vital sign monitoring [Nandakumar et al. 2019, 2015; Wang et al. 2017b]. With the embedded speaker and microphone, a smartphone can detect the movement of human chest from the reflected acoustic signal. Since the acoustic signal is not affected by the lighting condition, the system can detect human respiration in dark environments. Furthermore, since the system can be implemented with smartphones, the cost of the system is not high. However, the range of the smartphone-based acoustic signal system is limited by both the power of the speaker and the sensitivity of the microphone. Thus, it only works when the smartphone is close to the body, and measuring multiple users simultaneously will be a big challenge. It does not work for heart rate monitoring because the acoustic signal does not penetrate clothes and the human body well. Another low-cost system is also proposed to monitor the breathing rate by geophones when the user is sleeping [Jia et al. 2016, 2017]. With the connection to the bed, the breathing signal and human heartbeats can be captured by the geophone. The geophone-based system can achieve high accuracy and is easy to set up, but the system requires the user to sleep on the bed equipped with the devices. Thus, the geophone-based system is not suitable for other testing scenarios where the user is sitting or standing.

Recently, radio frequency (RF)-based vital sign monitoring has attracted great interest, which exploits wireless signals to detect breathing-induced chest movement. For example, the Vital-Radio system uses a frequency-modulated continuous wave (FMCW) radar to estimate breathing and heart rates [Adib et al. 2015]. It works for multiple subjects but requires a customized hardware operating on a large bandwidth from 5.46 to 7.25 GHz. Other techniques, such as Doppler radar [Droitcour et al. 2009; Nguyen et al. 2016] and ultra-wideband radar [Salmi and Molisch 2011], are also utilized to monitor vital signs. The mmVital system [Yang et al. 2016] uses the received signal strength (RSS) of 60-GHz millimeter wave (mmWave) signals for breathing and heart rate estimation. These systems all require a dedicated hardware and a large bandwidth on which to operate, leading to relatively high cost. A recent work, UbiBreathe, uses the RSS of WiFi signals to monitor the breathing signal [Abdelnasser et al. 2015]. RSS represents coarse channel information, and UbiBreathe requires the patient to be on the line of sight (LOS) path between the transmitter and receiver, which limits the RF monitoring range in deployment.

Unlike RSS, channel state information (CSI) represents fine-grained channel information, which is now available for several off-the-shelf WiFi network interface cards (NICs), such as Intel WiFi Link 5300 NIC [Halperin et al. 2010] and the Atheros AR9580 chipset [Xie et al. 2015]. Specifically, CSI consists of both subcarrier-level amplitude and phase information of the underlying orthogonal frequency division multiplexing (OFDM) channel. It is a more stable representation of channel characteristics than RSS. In a recent work, Liu et al. [2015] used WiFi CSI amplitude to monitor the vital signs of a sleeping person. In addition, the CSI phase is employed to estimate human vital signs in Wang et al. [2017d] and Zhang et al. [2019]. Different from CSI amplitude, it is harder to exploit the CSI phase for vital signal monitoring due to the large variations caused by environmental noise and the unsynchronized time and frequency between the transmitter and receiver.

In this article, we leverage CSI phase difference data from antenna pairs of the receiver NIC to accurately measure and monitor breathing rate and heart rate. We find that CSI phase difference is quite stable over time for a given location after suitable calibration. Moreover, CSI phase difference is also more robust than RSS in various deployment scenarios, such as different distances, obstacles/walls, and orientations. We provide a rigorous analysis of CSI phase difference data and prove that for indoor multipath environments under small-scale fading, the CSI phase difference data is a periodic signal with the same frequency as the breathing signal when the WiFi signal is reflected from the chest of a person.

Built upon the analysis, we design PhaseBeat, a remote sensing system using CSI phase difference data for monitoring respiration and heartbeat with a commodity WiFi device. First, PhaseBeat exploits CSI phase difference to extract the periodic signal induced by chest movements (e.g., inhaling and exhaling). Then, PhaseBeat preprocesses the captured data, with environment detection, data calibration, subcarrier selection, and discrete wavelet transform (DWT). For environment detection, PhaseBeat detects whether the patient is in a stationary stage, such as sitting, standing, and sleeping, using a threshold-based method. Then, effective phase difference data is calibrated by removing the direct current (DC) component and high-frequency noise, and by downsampling the processed data. Due to frequency diversity, the most sensitive subcarrier is selected and processed by DWT to obtain the denoised breathing signal and the reconstructed heart signal. Finally, we apply a peak detection method for breathing rate measurement and a fast Fourier transform (FFT)-based method for heart signal estimation.

We prototype PhaseBeat with off-the-shelf WiFi devices and evaluate its performance with extensive experiments. The experiments involve four persons over a period of 3 months in typical indoor environments, such as a computer laboratory, a through-wall scenario, and a long corridor. The experimental results demonstrate that PhaseBeat can achieve high accuracy for breathing and heart rate estimation, with a median error of 0.25 breaths per minute (bpm) and 1.19 bpm for breathing rate and heart rate, respectively. We also find PhaseBeat highly robust for breathing rate estimation under various environments, such as different distances, different orientations and poses, and multiple persons.

1.1 Summary of Main Contributions

The main contributions of this article are summarized as follows. First, we theoretically and experimentally validate the feasibility of using CSI phase difference for vital sign monitoring. Different from other CSI-based techniques, we provide a rigorous analysis of the measured CSI phase signal with respect to its stability and periodicity. To the best of our knowledge, this is the first work to exploit CSI phase difference for both breathing rate and heart rate estimation [Wang et al. 2017d]. Second, the PhaseBeat system is designed based on the analysis of CSI phase difference. We develop several signal processing algorithms for preprocessing the collected CSI phase difference data, which can obtain the denoised breathing signal and the reconstructed heart signal. Wavelet techniques are implemented to separate heartbeat signal from respiration signal. Then, we employ peak detection and root-MUSIC methods for breathing rate estimation for one and multiple persons, respectively, and leverage an FFT-based method for heart rate estimation. Third, we prototype the PhaseBeat system with commodity WiFi devices and validate its superior performance in several typical indoor environments with extensive experiments. We also investigate the impact of different factors by the experiments such as distance, orientations, and poses. Our experimental results demonstrate the superior performance of PhaseBeat over state-of-the-art baseline schemes.

1.2 Organization

In the remainder of this article, we present the preliminaries and our analysis of phase difference data in Section 2. We describe PhaseBeat design in Section 3 and demonstrate its performance in Section 4. Section 5 discusses related work, and Section 6 concludes the work.

2 PRELIMINARIES AND PHASE DIFFERENCE ANALYSIS

2.1 Channel State Information

OFDM is widely used in modern wireless network standards, such as WiFi (i.e., IEEE 802.11a/g/n). With OFDM, the total spectrum is partitioned into multiple orthogonal subcarriers, and data is transmitted over the subcarriers using inverse fast Fourier transform (IFFT) to mitigate frequency selective fading. Leveraging the device driver for off-the-shelf NICs, such as the Intel 5300 NIC [Halperin et al. 2010], we can extract CSI from the NIC for each

received packet, which is fine-grained physical layer (PHY) information. CSI reveals the channel characteristics experienced by the received packet, such as the multipath effect, shadow fading, and distortion [Wang et al. 2015, 2016].

With OFDM, the WiFi channel at the 5-GHz band can be considered as a narrowband flat fading channel. In the frequency domain, the channel model can be expressed as $\vec{Y} = \text{CSI} \cdot \vec{X} + \vec{N}$, where $\vec{Y}$ and $\vec{X}$ denote the received and transmitted signal vectors, respectively, $\vec{N}$ is the additive white Gaussian noise (AWGN), and CSI represents the channel's frequency response, which can be estimated from $\vec{Y}$ and $\vec{X}$.

Although the WiFi OFDM system has 56 subcarriers over a 20-MHz channel, the Intel 5300 NIC can report CSI for only 30 of the 56 subcarriers. The channel frequency response of subcarrier i, CSI_i, is a complex value, which is

$$\text{CSI}_i = \mathcal{I}_i + j\mathcal{Q}_i = |\text{CSI}_i| \exp\left(j\angle \text{CSI}_i\right), \tag{1}$$

where $\mathcal{I}_i$ and $\mathcal{Q}_i$ are the in-phase component and quadrature component, respectively; $|\text{CSI}_i|$ and $\angle \text{CSI}_i$ are the amplitude response and phase response of subcarrier i, respectively.

For an indoor environment with NLOS components [Yang et al. 2013], the frequency response of subcarrier i can also be written as

$$\text{CSI}_i = \sum_{k=1}^{K} r_k \cdot \exp\{-j2\pi f_i \tau_k\}, \tag{2}$$

where K is the number of multipaths; r_k and τ_k are the attenuation and the propagation delay from the k_{th} path, respectively; and f_i is the central frequency of subcarrier i. Traditionally, the multipaths are harmful for indoor localization, because only the LOS component is a good indicator of distance [Xiong and Jamieson 2013; Yang et al. 2013]. However, our PhaseBeat system can effectively exploit the reflections for vital signal monitoring, as will be shown in the remainder of this article.

2.2 Phase Difference

In this section, we show that the difference of CSI phase values between two antennas of the 5-GHz OFDM channel is highly stable over time. Although the CSI phase information is available from the Intel 5300 NIC, it is usually highly random and cannot be directly used for vital sign monitoring due to noise and the unsynchronized time and frequency of the transmitter and receiver. Recently, two useful algorithms were used to remove the randomness in the CSI phase. The first approach is to make a linear transform of the phase values measured from the 30 subcarriers [Qian et al. 2014; Wang et al. 2016]. The other is to exploit the phase difference between two antennas in the 2.4-GHz band and then remove the measured average [Wu et al. 2015]. Although both methods can stabilize the CSI phases collected from consecutively received packets, the average phase value that they produce is always near zero, which is different from the real phase value of the received signal.

We now provide an analysis to validate the stability of the measured phase difference. Let $\widehat{\angle CSI}_i$ denote the measured phase of subcarrier i, which is given in other works [Mao et al. 2016; Speth et al. 1999; Wang et al. 2017c, 2017e; Xie et al. 2015]:

$$\widehat{\angle CSI}_i = \angle \text{CSI}_i + (\lambda_p + \lambda_s)m_i + \lambda_c + \beta + Z, \tag{3}$$

where $\angle \text{CSI}_i$ is the true phase value; m_i is the real subcarrier index of the ith subcarrier in the set that can be read by the device driver; β is the initial phase offset due to the phase-locked loop (PLL); Z is the measurement noise that is assumed to be AWGN of variance σ^2; and λ_p, λ_s, and λ_c are the phase errors introduced by the packet boundary detection (PBD), the sampling frequency offset (SFO), and the central frequency offset (CFO),

respectively [Speth et al. 1999]. These phase errors can be written as

$$
\begin{cases}
\lambda_p = 2\pi \left(\frac{\Delta t}{N} \right) \\
\lambda_s = 2\pi n \left(\frac{T'-T}{T} \right) \left(\frac{T_s}{T_u} \right) \\
\lambda_c = 2\pi \Delta f T_s n,
\end{cases}
\tag{4}
$$

where Δt is the PBD delay; N is the FFT size; T' and T are the sampling periods at the receiver and the transmitter, respectively; T_u is the length of the data symbol; T_s is the total length of a data symbol and the guard interval; n is the sampling time offset for the current packet; and Δf is the center frequency difference between the transmitter and receiver. Note that we cannot obtain the exact values for Δt, $\frac{T'-T}{T}$, n, Δf, and β in (3) and (4). Moreover, λ_p, λ_s, and λ_c vary for different packets that have different Δt and n. Thus, the true phase $\angle\text{CSI}_i$ cannot be obtained from the measured phase value. Fortunately, the measured *phase difference* on subcarrier i can be leveraged as in the following theorem.

THEOREM 2.1. *The measured phase difference on subcarrier i between two receiver antennas, denoted by $\Delta\angle\widehat{CSI}_i$, is more stable than measured phase, and its mean and variation are given by*

$$
\begin{cases}
\mathbb{E}(\Delta\angle\widehat{CSI}_i) = \mathbb{E}(\Delta\angle CSI_i) + \Delta\beta \\
\text{Var}(\Delta\angle\widehat{CSI}_i) = \text{Var}(\Delta\angle CSI_i) + 2\sigma^2,
\end{cases}
\tag{5}
$$

where $\Delta\angle CSI_i$ is the true phase difference of subcarrier i, $\Delta\beta$ is the unknown difference in phase offsets, which is in fact a constant [Gjengset et al. 2014], and σ^2 is the variance of noise Z.

PROOF. Note that the three antennas of the Intel 5300 NIC use the same clock and the same down-converter frequency. Consequently, the measured phases of subcarrier i from two antennas, denoted as having identical packet detection delay, sampling periods, frequency differences, and the same index m_i [Gjengset et al. 2014]. Thus, the measured phase difference on subcarrier i between two antennas can be approximated as

$$
\Delta\angle\widehat{CSI}_i = \Delta\angle\text{CSI}_i + \Delta\beta + \Delta Z,
\tag{6}
$$

where ΔZ is the noise difference. Since Δt, Δf, and n are all removed, $\Delta\angle\widehat{CSI}_i$ in (6) becomes more stable over consecutive received packets than the measured phase. From (6), we can derive the mean and variance of the measured phase difference on subcarrier i as that given in (5). □

From (5), it can be seen that $\mathbb{E}(\Delta\angle\widehat{CSI}_i) - \mathbb{E}(\Delta\angle CSI_i)$ is a constant $\Delta\beta$. The difference does not change the estimated frequency of vital signals, although its variance becomes twice the noise variance. Figure 1 plots the phases read from a single antenna (as blue crosses) and the phase differences read from a pair of antennas (as red dots) on the fifth subcarrier in the polar coordinate system for 600 consecutively received packets. We can see that the single antenna phase is nearly uniformly distributed between $0°$ and $360°$; obviously, it is not stable over time. However, all phase difference data concentrate into a sector between $190°$ and $210°$, which clearly validates Theorem 2.1.

In the following lemma, we show that the measured phase difference information is periodic.

LEMMA 2.2. *When the WiFi signal is reflected from the chest of a patient, who is breathing at a rate of f_b bpm, the true phase of the reflected signal received at any antenna of the receiver is also periodic with the same rate f_b.*

PROOF. Assuming the WiFi signal on subcarrier i is a plane wave, its true phase at the receiver is determined by the propagation distance—that is, $\angle\text{CSI}_i = 2\pi d(t)/\lambda_i$, where $d(t)$ is the propagation distance at time t and λ_i is the wavelength of subcarrier i. When the chest periodically rises and falls at frequency f_b, the propagation distance $d(t)$ of the reflected signal becomes $d(t) = D + A\cos(2\pi f_b t)$, where D is the constant, mean distance of
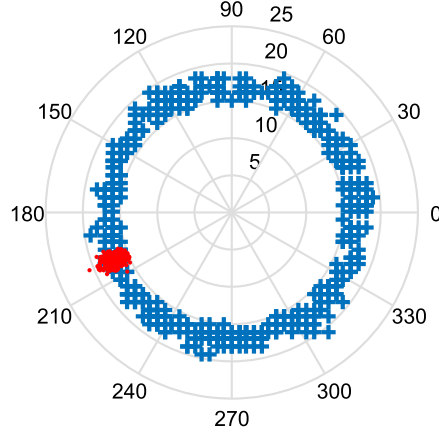
Fig. 1. Comparison between phase CSI measured from a single antenna (marked as blue crosses) and the phase differences measured from two antennas (marked as red dots) of the fifth subcarrier for 600 consecutively received packets.

the reflection path and A is the amplitude of chest movements. Thus, the true phase of the reflected signal at the receiver is

$$\angle\text{CSI}_i = \frac{2\pi}{\lambda_i}(D + A\cos(2\pi f_b t)). \tag{7}$$

Thus, the true phase is a periodic signal with frequency f_b. □

THEOREM 2.3. *For an indoor environment with multipaths, when the WiFi signal is reflected from the chest of a patient who is breathing at a frequency f_b, the true phase received at any antenna of the receiver is also a periodic signal with a frequency f_d such that*

$$P\left(|f_d - f_b| < \epsilon\right) = 1, \quad \forall \epsilon > 0. \tag{8}$$

PROOF. Based on Lemma 2.2, the true phase of the reflected signal at the receiver, $\angle\text{CSI}_i = 2\pi(D + A\cos(2\pi f_b t))/\lambda_i$ is periodic with frequency f_b. Let the reflected signal be a *dynamic component* and the sum of the LOS and other multipath signals as a *static component*. We can rewrite (2) as

$$\text{CSI}_i = \sum_{k=1,\,k\neq d}^{K} r_k \cdot \exp\{-j2\pi f_i \tau_k\} + r_d \cdot \exp\{-j2\pi f_i \tau_d\}$$

$$= |\text{CSI}_i^s| \exp\left(j\angle\text{CSI}_i^s\right) + |\text{CSI}_i^d| \exp\left(j\angle\text{CSI}_i^d\right), \tag{9}$$

where $\text{CSI}_i^s = \sum_{k=1,\,k\neq d}^{K} r_k \cdot \exp\{-j2\pi f_i \tau_k\}$ is the static component and $\text{CSI}_i^d = r_d \cdot \exp\{-j2\pi f_i \tau_d\}$ is the dynamic component. Moreover, $\angle\text{CSI}_i^d$ is a periodic signal with frequency f_b, and $|\text{CSI}_i^s|$, $\angle\text{CSI}_i^s$, and $|\text{CSI}_i^d|$ are considered to be constants if there are no other movements in the neighborhood.

To obtain the phase of CSI_i, we illustrate the geometric relationship of the static component CSI_i^s, the dynamic component CSI_i^d, and the total component CSI_i using an *in-phase-quadrature* (I-Q) plot, as shown in Figure 2. From this figure, we can easily obtain the angle $\angle\text{DST} = \angle\text{CSI}_i^s - \angle\text{CSI}_i^d$. The length of segment $OT = |\text{CSI}_i^d|\cos(\angle\text{CSI}_i^s - \angle\text{CSI}_i^d) + |\text{CSI}_i^s|$, and the length of segment $TD = |\text{CSI}_i^d|\sin(\angle\text{CSI}_i^s - \angle\text{CSI}_i^d)$. The phase of the total component CSI_i can be computed as

$$\angle\text{CSI}_i = \angle\text{CSI}_i^s - \arctan\left(\frac{|\text{CSI}_i^d|\sin(\angle\text{CSI}_i^s - \angle\text{CSI}_i^d)}{|\text{CSI}_i^d|\cos(\angle\text{CSI}_i^s - \angle\text{CSI}_i^d) + |\text{CSI}_i^s|}\right). \tag{10}$$
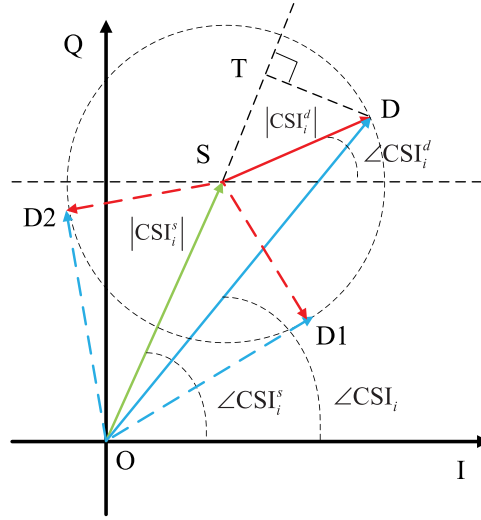
Fig. 2. Illustration of the geometric relationship among the static component CSI_i^s (the green vector $\overline{OS}$), the dynamic component CSI_i^d (the red vector $\overline{SD}$), and the total component CSI_i (the blue vector $\overline{OD}$) in the I-Q plot.

Because $\angle CSI_i^d$ is periodic, $\angle CSI_i$ is also periodic. To show that the frequency of the total phase $\angle CSI_i$ is f_b, we differentiate (10) and set the derivative to zero. We then have

$$\cos(\angle CSI_i^s - \angle CSI_i^d) = -\frac{|CSI_i^d|}{|CSI_i^s|}. \tag{11}$$

The solution is $\angle CSI_i^d = \angle CSI_i^s + \pi - \arccos(|CSI_i^d|/|CSI_i^s|)$ (vector $\overrightarrow{SD_2}$) or $\angle CSI_i^d = \angle CSI_i^s + \pi + \arccos(|CSI_i^d|/|CSI_i^s|)$ (vector $\overrightarrow{SD_1}$), as shown in Figure 2. When the phase is in the range as

$$\angle CSI_i^d \in \{\angle CSI_i^s + \pi + \arccos(|CSI_i^d|/|CSI_i^s|) - 2\pi, \angle CSI_i^s + \pi - \arccos(|CSI_i^d|/|CSI_i^s|)\},$$

Equation (10) is an increasing function; otherwise, it is a decreasing function. Thus, except for the only two positions $\overrightarrow{SD_1}$ and $\overrightarrow{SD_2}$, the phase of the total component CSI_i is periodic with frequency f_b. Moreover, since the true phase CSI_i is continuous, the probability that the true phase CSI_i stays exactly at positions $\overrightarrow{SD_1}$ and $\overrightarrow{SD_2}$ equals to zero. Thus, Theorem 2.3 holds true. □

Now consider another antenna. With the same analysis, we can also obtain (10) for the additional antenna, which is also periodic with frequency f_b. However, its the static component CSI_i^s and the dynamic component CSI_i^d on subcarrier i that are different due to different positions of the two antennas. This is true for any pair of antennas of the Intel 5300 NIC. We thus conclude that the true phase difference between any pair of antennas is a periodic signal with the frequency f_b.

Following Theorem 2.1 and (6), we can easily show that the measured phase difference on subcarrier i between two antennas is also a stable periodic signal with frequency f_b, although the waveform of the signal is attenuated due to increased noise. To improve the signal waveform, directional antennas can be used at the transmitter, which can strengthen the power of the reflected signal from the chest. In the PhaseBeat system, we adopt a directional antenna at the transmitter for heart rate monitoring, because the heartbeat introduced effect on the reflected signal is extremely weak.
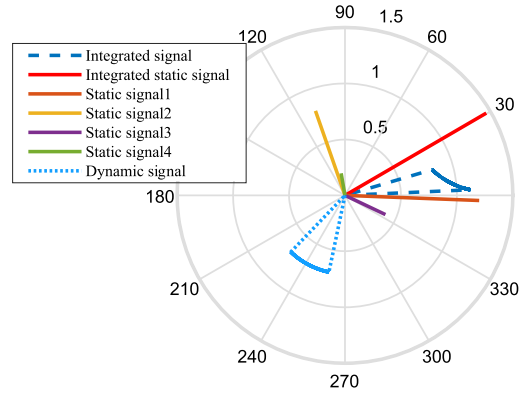
Fig. 3. Illustration of the combined signal and its components of one dynamic signal and four static signals.
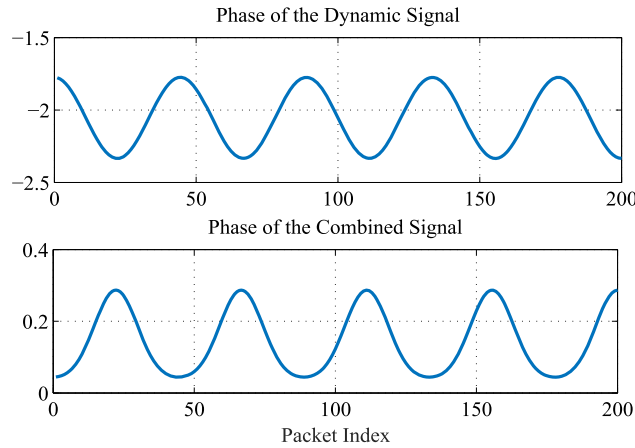

Fig. 4. Illustration of the phases of the periodic dynamic component and the combined signal.

As an example of (9), we show a numerical result in Figure 3. There are four static components due to mutipath and one dynamic component caused by human respiration. All of these components are shown as complex vectors in the polar coordinate. The strength of static components decreases from the first component to the fourth, and the phases of these four static components are all set as random number from-π to π. Then the combined static vector is plotted as the red line. The dynamic component is showed as a blue sector, which means that the phase of dynamic component changes periodically in a certain region and the strength is considered to be a constant. The final integrated vector is the combination of the dynamic vector and the integrated static vector, which is represented in dark blue. The numerical result represents that the phase of the integrated signal still varies in a certain range, although the combined signal is affected by the different static components caused by the multipath effect.

Following the numerical results shown in Figure 3, we show the phase changes of the dynamic signal and the final combined signal in Figure 4. It can be seen that when the phase of the dynamic signal varies periodically between −1.79 and −2.38, the phase of the overall integrated signal also varies periodically from 0.05 to 0.28. Even though the shape of the combined signal is not perfect sinusoidal, the period of this signal is apparently equal to the period of the dynamic signal, as given in Theorem 2.3.

To reveal the effect of directional antennas, we derive the following corollaries based on Theorem 2.3 and (10).
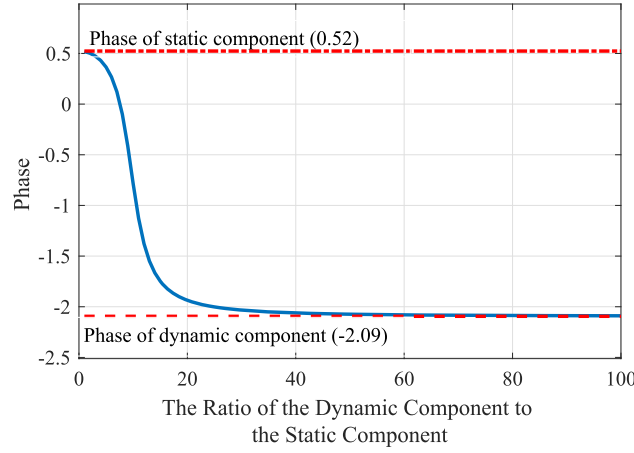
Fig. 5. Numerical results to show the impact of the ratio of the dynamic and static components.

COROLLARY 2.3.1. *When the ratio $|CSI_i^d|/|CSI_i^s| \to \infty$, the true phase of subcarrier i at a receiver antenna becomes a periodic signal with frequency f_b, and the true phase of subcarrier i becomes $\angle CSI_i = \angle CSI_i^d$.*

PROOF. According to (10), it can be easily shown that $\angle CSI_i = \angle CSI_i^d$ when the ratio $|CSI_i^d|/|CSI_i^s| \to \infty$. Moreover, $\angle CSI_i^d$ is a periodic signal with frequency f_b. Therefore, the corollary is proven. □

COROLLARY 2.3.2. *When the ratio $|CSI_i^d|/|CSI_i^s| \to 0$, the true phase of subcarrier i at a receiver antenna will not be periodic, and the true phase of subcarrier i becomes $\angle CSI_i = \angle CSI_i^s$.*

PROOF. According to (10), it can be easily shown that $\angle CSI_i = \angle CSI_i^s$, when the ratio $|CSI_i^d|/|CSI_i^s| \to 0$. Moreover, $\angle CSI_i^s$ is not a periodic signal. Thus, the corollary is proven. □

Following Corollaries 2.3.1 and 2.3.2, it can be seen that when the chest reflection is strong, the waveform of the received signal becomes periodic with a high SNR; when the chest reflection is weak, the waveform of the received signal is still periodic but with a low SNR. Thus, it is still challenging to estimate the breathing rate and heart rate from the reflected signal due to the multipath effect, obstacles, a long distance between the person and the WiFi devices, and the low SNR.

Figure 5 shows that our numerical results validate Corollaries 2.3.1 and 2.3.2. We change the strength of the integrated static component, as shown in Figure 3, to achieve different ratios of $|CSI_i^d|/|CSI_i^s|$. The phase of the integrated static vector is 0.52, and the mean phase of the periodic dynamic vector is -2.09. When the ratio is zero, the angle of the integrated vector is equivalent to the static vector angle. As the ratio is increased from zero to 100, the angle of the integrated vector decreases rapidly and approaches the dynamic vector angle. Using a directional antenna can effectively increase the ratio $|CSI_i^d|/|CSI_i^s|$ and helps to improve the accuracy of PhaseBeat.

3 THE PHASEBEAT SYSTEM

3.1 PhaseBeat System Architecture

We designed the PhaseBeat system to monitor vital signs, including breathing and heartbeat, of one or more persons by leveraging CSI phase difference data with commodity WiFi devices. Specifically, PhaseBeat exploits CSI phase difference data to extract the periodic signal caused by the rise and fall of the chest (e.g., inhaling and
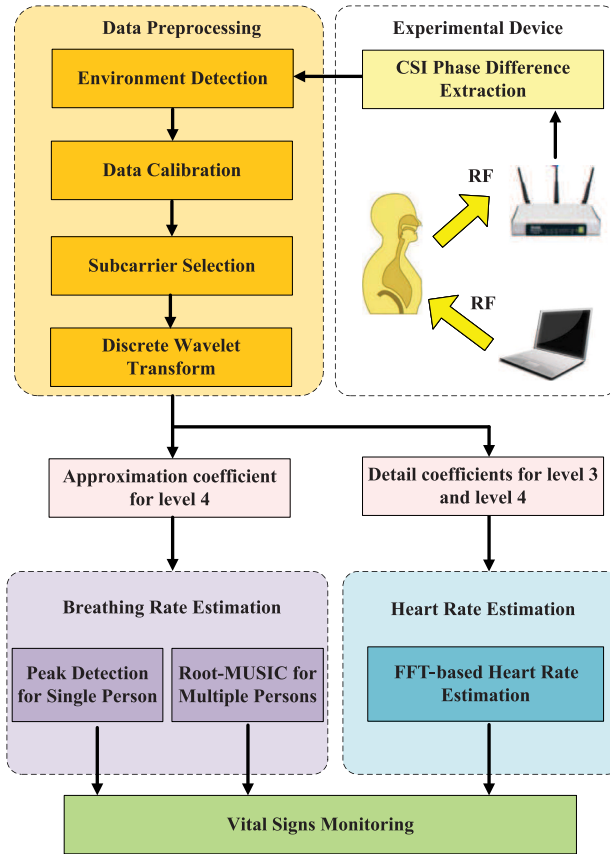
Fig. 6.   PhaseBeat system architecture.

exhaling). Based on Theorems 2.1 and 2.3, PhaseBeat can effectively exploit CSI phase difference data to monitor vital signs. As discussed, CSI phase difference is relatively stable over time (i.e., as sampled by back-to-back WiFi packets) in stationary environments. It can thus be effective for monitoring vital signs. Furthermore, CSI phase difference carries a periodic signal that has the same frequency as the breathing signal. Finally, CSI phase difference is more resilient compared to CSI amplitude used in prior work for monitoring vital signs.

The PhaseBeat system architecture is presented in Figure 6. It includes four basic modules: Data Extraction, Data Preprocessing, Breathing Rate Estimation, and Heart Rate Estimation. The Data Extraction module collects CSI phase difference data between two receiver antennas of an off-the-shelf WiFi device. The Data Preprocessing module consists of environment detection, data calibration, subcarrier selection, and DWT. The environment detection module applies a threshold method to determine the stationary state of the person, such as sitting, standing, or sleeping. For data calibration, we remove the DC component and high-frequency noises, and down-sample the processed data. Then, subcarrier selection is applied to improve the reliability of CSI phase difference data. The DWT is used to obtain the denoised breathing signal and the reconstructed heart signal in different frequency ranges. In the Breathing Rate Estimation module, we measure the breathing rate using peak detection for the case of a single person and the root-MUSIC method for multiple persons. In the Heart Rate Estimation module, we apply an FFT-based method to detect the heart rate.
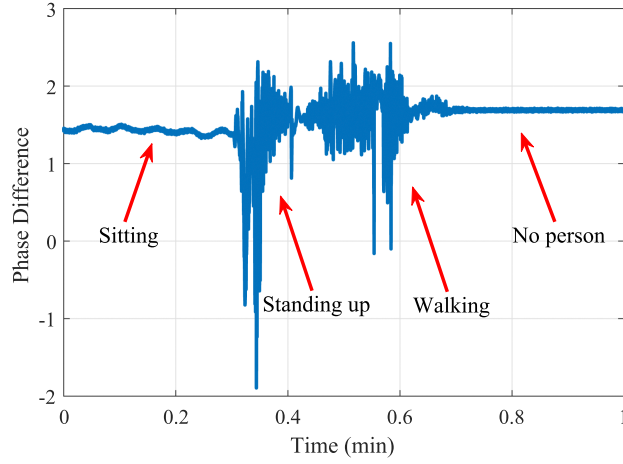
Fig. 7. Detection of the monitoring environment to see if the collected phase difference data is usable.

3.2 Data Preprocessing

3.2.1 Environment Detection. After extracting CSI phase difference information using (6), we need to determine whether the person is in a stationary state (i.e., if the data is usable). When the person is determined to be in a stationary state, no matter whether the person is sitting, standing, or sleeping, PhaseBeat can estimate the breathing rate and heart rate. A threshold-based method is used to identify whether a segment of CSI phase difference data is received in a stationary state by evaluating the mean absolute deviation of the CSI phase difference data in a short sliding window.

Define V as the sum of mean absolute deviations of all CSI phase difference data in the sliding window as

$$V = \frac{1}{|W|} \sum_{k \in W} \sum_{i=1}^{30} |\Delta\angle\widehat{CSI}_i(k) - \mathbb{E}(\Delta\angle\widehat{CSI}_i(k))|, \qquad (12)$$

where $\Delta\angle\widehat{CSI}_i(k)$ is the phase difference from subcarrier i collected from the kth received packet, W is the index set of all packets in the sliding window, and $|W|$ is the cardinality of the sliding window. Because other movements lead to larger variations in CSI phase difference data than that caused by the minute movements of breathing and heartbeat, the threshold-based approach is effective in detecting such large movements (e.g., walking or jumping). In PhaseBeat, we set the threshold between 0.25 and 6 to identify useful data for vital sign monitoring.

Figure 7 presents the environment detection results for different states. When the person is sitting, the phase difference data is a sinusoidal-like periodic signal over time. When there is no one in the range, the phase difference data is a straight line with very small fluctuations. When the person stands up or is walking, the phase difference data exhibits much larger fluctuations. Thus, a simple threshold can be effective to determine the stationary state of the person.

3.2.2 Data Calibration. To obtain robust CSI phase difference data, we further calibrate the data to remove the DC component and high-frequency noises, and to downsample the processed data. The DC component affects subcarrier selection, peak detection, and FFT frequency estimation. Thus, PhaseBeat needs to remove the DC component with a *Hampel filter*. Unlike traditional data calibration methods that only remove high-frequency noises, we use the Hampel filter for detrending of the original CSI phase difference data. The Hampel filter is utilized to obtain the basic trend of the original data, which is set as a large sliding window with 2,000 samples and a small threshold of 0.01. Then, the detrended data is obtained by subtracting the basic trend from the
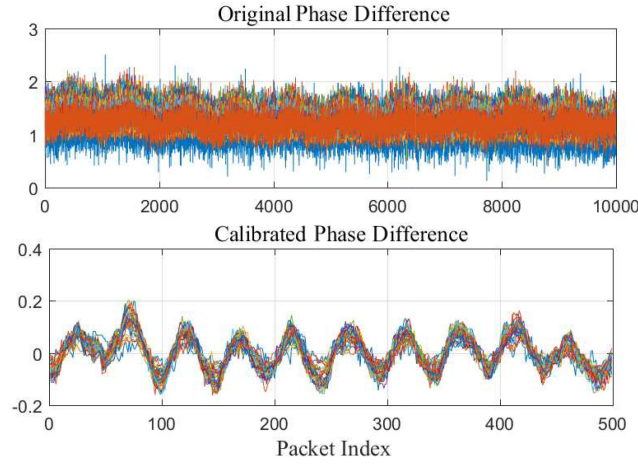
Fig. 8. Data calibration results.

original data. In addition, we also leverage the Hampel filter to reduce high-frequency noises using a smaller sliding window with 50 samples and the same threshold of 0.01.

In our prototype system, the PhaseBeat transmitter sends 400 WiFi packets per second to sample the chest movement (i.e., a sampling rate of 400 Hz). Since the normal heart rate and breathing rate are lower than 2 Hz, we downsample the data to reduce the computation complexity for real-time breathing and heart rate estimation. We use a downsampling rate of 20 to obtain lower-frequency CSI phase difference data, which is equivalent to sampling at 20 Hz.

Figure 8 presents the data calibration results. It can be seen that the original phase differences of all subcarriers have a DC component and high-frequency noises. By implementing the proposed data calibration scheme, both the DC component and high-frequency noises are greatly reduced; the CSI from each of the subcarriers becomes a sinusoidal-like periodic signal over the sampling packets. The number of samples is decreased from 10,000 to 500, which is amenable to applying the signal processing methods in the following modules.

Note that the transmitter and receiver of PhaseBeat consists of a stand-alone WiFi link. It can be configured to use a different channel than the surround WiFi network to avoid channel contention. Furthermore, as shown earlier, a reduced sampling rate of 20 Hz is sufficient for both respiration and heart rate monitoring. In addition, PhaseBeat does not require transmitting all the time. It can be configured to transmit at proper intervals. When there is normal data transmission between the transmitter/receiver, the CSI can be extracted and used, and there is no need to send sampling packets. Finally, for applications such as sleep monitoring, the WiFi activities are usually very low when PhaseBeat works. Thus, even if the same channel is used with the surrounding WiFi network, the interference introduced by PhaseBeat will be very limited.

3.2.3 Subcarrier Selection.
PhaseBeat employs subcarrier selection to further boost the reliability of CSI phase difference data. Different subcarriers have different wavelengths, leading to different sensitivities for breathing and heart signals. We use the mean absolute deviation of CSI phase difference data from every subcarrier to measure its sensitivity. In general, the larger the mean absolute deviation, the higher the sensitivity.

We first choose the top k subcarriers with the maximum mean absolute deviations of CSI phase difference data. Then, we choose the subcarrier that has the median of the k mean absolute deviations. Figure 9 shows the CSI phase difference series patterns after data calibration. We find that subcarriers 18 to 21 have a higher sensitivity to the breathing signal, since the phase difference on these subcarriers exhibits a periodic pattern of strong-weak fluctuations over the 600 sampling packets. In PhaseBeat, we set $k = 3$ as the default value, and subcarriers 19,
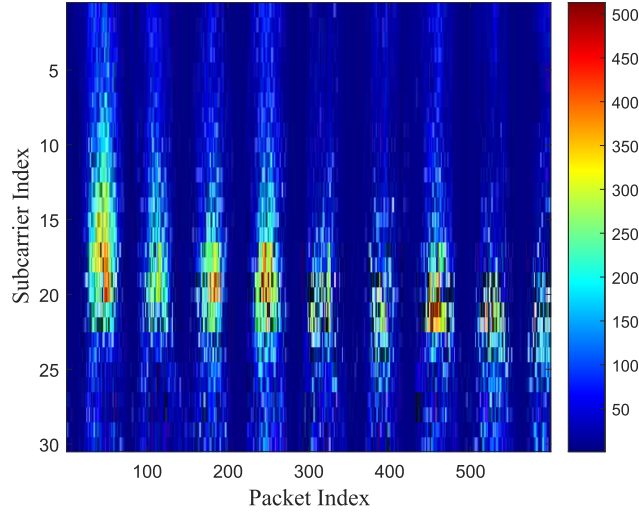
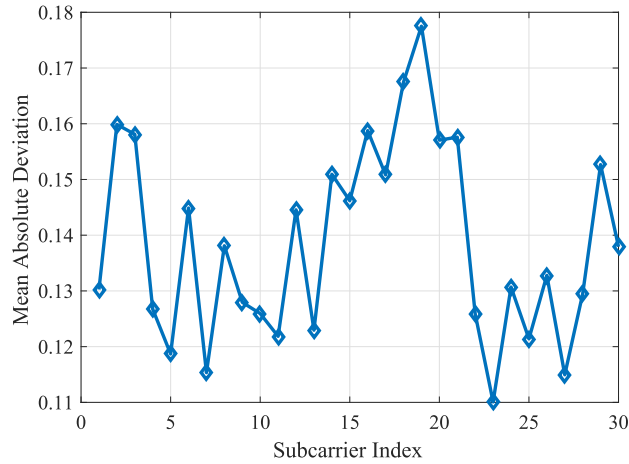Fig. 9. CSI phase difference series patterns after data calibration.

Fig. 10. Mean absolute deviation of each subcarrier.

18, and 2 are the top three with the largest mean absolute deviations. Subcarrier 18 is finally selected, which has the medium value among the top three, as shown in Figure 10. Since the wireless channel is relative stable when the user is not moving, the subcarriers are selected only at the beginning of the sensing period and/or when a large movement is detected by the environment detection module.

3.2.4 Discrete Wavelet Transform. Different from FFT and short-time Fourier transform (STFT), DWT can achieve a time-frequency representation of data, which provides not only the optimal resolution both in the time and frequency domains but also a multiscale analysis of the data. With DWT, the phase difference data after subcarrier selection can be decomposed into an *approximation coefficient* vector with a low-pass filter and a *detail coefficient* vector with a high-pass filter. In fact, the approximation coefficient vector represents the basic shape of the input signal with large-scale characteristics, whereas the detail coefficient vector describes the high-frequency noises and the detailed information with small-scale characteristics.
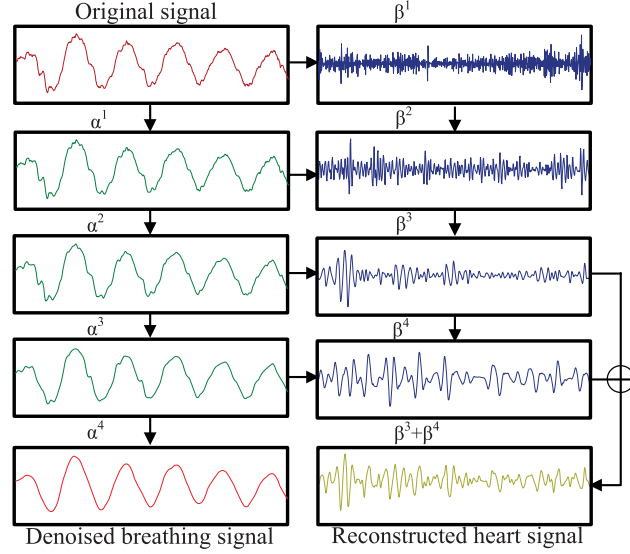
Fig. 11. DWT results.

In wavelet decomposition, the following steps recursively split the previous approximation coefficient and detail coefficient into two new coefficients based on the same scheme [Sardy et al. 2001]. After L steps, the DWT can obtain an approximation coefficient α^L and a sequence of detail coefficients $\beta^1, \beta^2, \ldots, \beta^L$. We can compute the DWT coefficients as follows:

$$\begin{cases} \alpha_k^{(L)} = \sum_{n \in \mathbb{Z}} \Delta\angle\widetilde{CSI}(n)\phi_{n-2^L k}^{(L)}, \ L \in \mathbb{Z} \\ \beta_k^{(l)} = \sum_{n \in \mathbb{Z}} \Delta\angle\widetilde{CSI}(n)\psi_{n-2^l k}^{l}, \ l \in \{1, \ldots, L\}, \end{cases} \tag{13}$$

where $\Delta\angle\widetilde{CSI}(n)$ is the phase difference after subcarrier selection, $\mathbb{Z}$ is the integer set, and the ϕ's and ψ's are wavelet basis functions, which are orthogonal to each other. The phase difference $\Delta\angle\widetilde{CSI}(n)$ can be approximated using inverse DWT, as follows:

$$\Delta\angle\widetilde{CSI}(n) = \sum_{k \in \mathbb{Z}} \alpha_k^{(L)}\phi_{n-2^L k}^{(L)} + \sum_{l=1}^{L} \sum_{k \in \mathbb{Z}} \beta_k^{(l)}\psi_{n-2^l k}^{l}. \tag{14}$$

In PhaseBeat, DWT is utilized to remove high-frequency noises from the collected CSI phase difference data. Moreover, the approximation coefficient α^L is used to detect the breathing rate, whereas the sum of detail coefficients $\beta^{L-1} + \beta^L$ is used to detect the heart rate. We set L to 4 in this article. As shown in Figure 11, for the original signal, we first execute the DWT-based decomposition recursively for four levels with the Daubechies (db) wavelet filter. After calibration, the sampling rate becomes 20 Hz. Then the sampling rate is halved after every step of DWT decomposition, and the detail coefficient β^1 and the approximation coefficient α^1 have a frequency ranging from 10 to 5 Hz and 0 to 5 Hz, respectively. After four decomposition steps, the approximation coefficient α^4 is in the range of 0 to 0.625 Hz, which is used to obtain the denoised breathing signal. The sum of detail coefficients $\beta^3 + \beta^4$ covers frequencies from 0.625 to 2.5 Hz, which is used to reconstruct the heart signal.

3.3 Breathing Rate Estimation

3.3.1 Peak Detection for the Single-Person Case. The breathing signal is caused by the small, periodic movement of inhaling and exhaling, which can be extracted from the phase difference data according to Theorem 2.3.
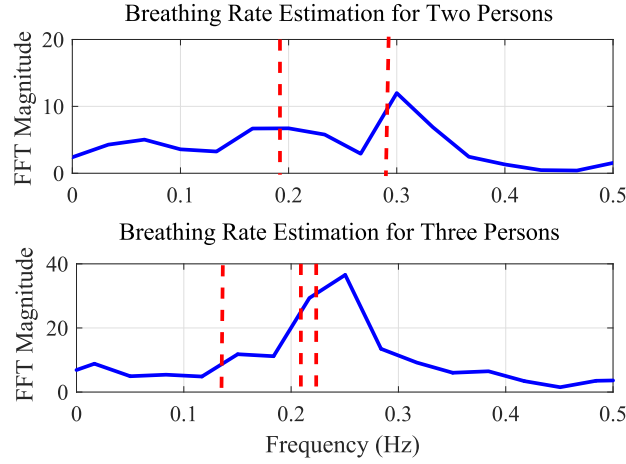
Fig. 12. Breathing rate estimation results for two persons (the upper plot) and three persons (the lower plot) based on FFT.

Although the FFT-based method can be used to estimate the breathing rate, its accuracy may not be good. This is because the frequency resolution depends on the window size of FFT. If the window size becomes larger, the estimation accuracy will be higher, but the time domain resolution will also be lower. Therefore, our Phase-Beat system employs peak detection to estimate the breathing rate based on the approximation coefficient α^L to achieve a high accuracy.

However, we find that the approximation coefficient α^L still contains fake peaks (i.e., local maximums). We thus use the sliding window method to identify the true peaks, where the window size is set to 51 samples based on a human's maximum breathing period [Liu et al. 2015]. We can identify all of the true peaks by checking whether the sample at the center of the window is the maximum value within the window. After peak detection, all peak-to-peak intervals are averaged to obtain the period of the breathing signal, denoted as P. Finally, the estimated breathing rate can be computed as $60/P$ bpm.

3.3.2 Root-MUSIC for the Multiperson Case. It is challenging to estimate the breathing rates for multiple persons using the approximation coefficient α^L because the reflected components in the received signal are now from multiple independent chest movements. The peak-to-peak detection method would not be effective in this case, as the approximation coefficient α^L is not a clearly periodic signal anymore.

An FFT-based method can transform the approximation coefficient α^L from the time domain to the frequency domain to estimate the breathing frequencies for two persons in LOS environments. However, with more persons and in more cluttered environments, the FFT-based method usually leads to poor results, especially when the breathing rates are very close to each other. Figure 12 illustrates the breathing rate estimation results for two persons (the upper plot) and three persons (the lower plot) with the FFT-based method, where the red dotted lines mark the real breathing frequencies (i.e., the ground truth). We can see that the estimated frequencies for the two persons are 0.2 and 0.3 Hz, respectively, which are both quite accurate. However, for the case of three persons, the FFT curve only shows two peaks, and the estimated breathing rates are much less accurate.

To address this issue, we propose a root-MUSIC-based method to estimate multiple breathing rates using phase difference data [Rao and Hari 1989]. The root-MUSIC method is effective for estimating the frequencies of signals consisting of a sum of sinusoids with AWGN [Rao and Hari 1989]. Specifically, we leverage 30 CSI phase difference series patterns after data calibration to build an *estimated correlation matrix* $\widehat{\mathbf{R}}$, which is given by
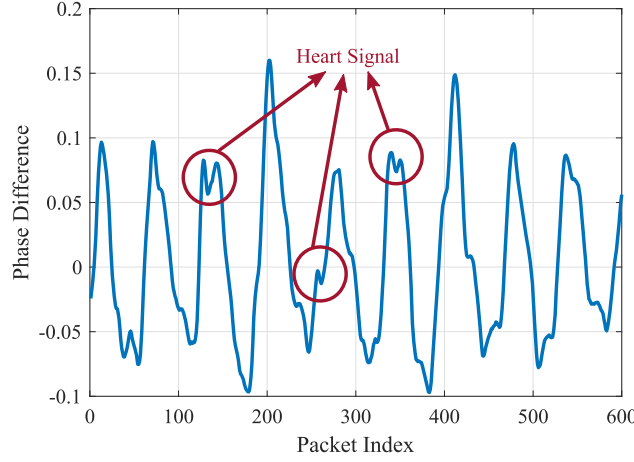
$$\widehat{\mathbf{R}} = \mathbf{H}\mathbf{H}^T,\tag{15}$$

Fig. 13. Heartbeats hidden in the breathing signal.

where **H** is a $I \times 30$ matrix that represents 30 CSI phase difference series after data calibration, which is defined as

$$\mathbf{H} = \begin{bmatrix} h_1(1) & h_2(1) & \cdots & h_{30}(1) \\ h_1(2) & h_2(2) & \cdots & h_{30}(2) \\ \vdots & \vdots & \cdots & \vdots \\ h_1(I) & h_2(I) & \cdots & h_{30}(I) \end{bmatrix}, \tag{16}$$

where $h_i(j)$ is the phase difference from subcarrier i for packet j after data calibration and I is the total number of sampling packets. After obtaining the estimated correlation matrix **R**, we incorporate the standard root-MUSIC method to obtain multiple persons' breathing rates. For the same phase difference data for three persons used in Figure 12, the breathing frequencies estimated by the proposed root-MUSIC-based method are 0.1467, 0.2233, and 0.2483 Hz, respectively, which are much more accurate than those estimated by the FFT-based method. Moreover, the proposed root-MUSIC-based method can effectively distinguish between two breathing signals with close breathing rates.

3.4 Heart Rate Estimation

3.4.1 FFT-Based Heart Rate Estimation. Heart rate is an important indicator of a person's health condition. Similar to the breathing signal, the heartbeat signal is also periodic, but the movement of the heart (i.e., diastole and systole) only causes very small variations in the chest-reflected signal. Figure 13 shows an example of heart signals hidden in the calibrated signal. In the figure, the respiration signal is quite obvious, whereas the small peaks generated by heartbeats are hardly visible. Thus, the peak detection method may not effectively extract the heartbeat signal from the collected CSI data. Moreover, the much stronger breathing signal also generates harmonics, which become strong interferences to the heart signal. It is thus more challenging to detect the heart rate than the breathing rate.

In PhaseBeat, we employ a directional antenna at the transmitter to improve the strength of the chest-reflected signal. Then, the sum of the detail coefficients $\beta^{L-1} + \beta^L$ of wavelet decomposition is utilized to estimate the heart rate. When the level of decomposition is $L = 4$, the frequency range is between 0.625 and 2.5 Hz, which filters out the breathing signals, which are between 0.17 and 0.62 Hz, as well as higher-frequency noises. Finally, we apply an FFT-based method to transform the sum of the detail coefficients $\beta^{L-1} + \beta^L$ to the frequency domain to estimate heart rate. To improve the frequency resolution, we adopt the method proposed in Adib et al. [2015]
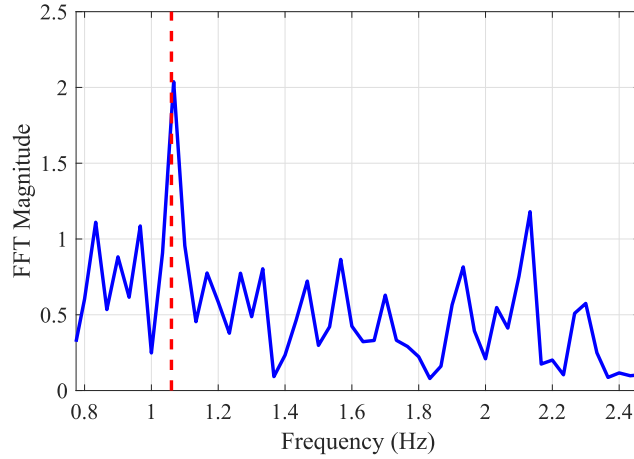
Fig. 14. Heart rate estimation using the FFT-based method.

Table 1. Impact of Different Antenna Types on Breathing
Rate and Heart Rate Estimation

Estimation Error	Omnidirectional Antenna	Directional Antenna
Breathing rate	0.23 bpm	0.25 bpm
Heart rate	4.82 bpm	1.19 bpm

for heart rate estimation. After finding the peaks in the FFT signal, we use three bins, including the peak bin and its two adjacent bins, where an inverse FFT is performed to obtain a complex time domain signal. The heart rate is estimated by evaluating the phase of the signal. Figure 14 illustrates heart rate estimation with the FFT-based method. The PhaseBeat estimated heartbeat frequency is 1.07 Hz, whereas heartbeat frequency measured by a commercial fingertip pulse sensor is 1.06 Hz. The heart rate estimated error is 0.01 Hz, or 0.6 bpm, in this experiment.

To further demonstrate the necessity of a directional antenna, we experimented with different types of antennas. The results are presented in Table 1. From the table, we can observe that the estimation error is similar for breathing rate estimation for different antenna types, which are 0.23 and 0.25 bpm, respectively. However, the error of heart rate is increased from 1.19 to 4.82 bpm, and the directional antenna is replaced by an omnidirectional antenna. This is because the power of the reflected signal from the heart is not large enough for accurate detection when the omnidirectional antenna is used.

4 EXPERIMENTAL STUDY

4.1 Test Configuration

In this section, we present our extensive experimental study with PhaseBeat in the 5-GHz band. In the experiments, we use a desktop computer configured as an access point and a Lenovo laptop as a mobile device, both equipped with the Intel 5300 NIC.[1] Our PhaseBeat system is implemented on the Ubuntu desktop 14.04 LTS OS for both the access point and the mobile device. The access point operates in the *monitor mode*, and the distance

---

[1]The resolution can be improved by using more antennas, and using an antenna array will certainly be beneficial. In this work, we build our system with commodity WiFi devices, which usually support three antennas. More antennas could be added, but additional equipment/hardware will be required to expand the interfaces and synchronize the antennas.
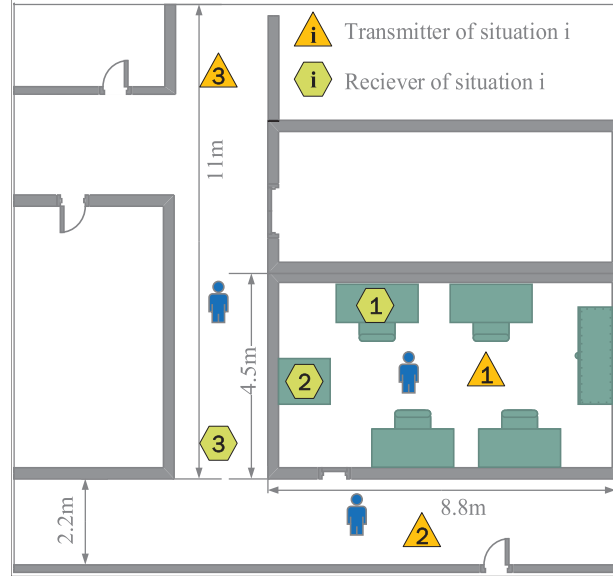
Fig. 15. Experimental scenarios of PhaseBeat performance evaluation.

between two adjacent antennas is $d = 2.68$ cm, which is half of the wavelength. The mobile device operates in the *injection mode* to transmit packets at 400 packets per second using only one antenna. Then, we extract CSI phase difference data between pairs of antennas at the access point for vital signal estimation.

We conducted extensive experiments on PhaseBeat. The experiments involved four persons, including three men and one woman. One of the male volunteers was 30 years old, whereas all other volunteers were 26 years old. The experiments were conducted within a period of 3 months. The test environments included a computer laboratory and corridors in Broun Hall of the Auburn University campus, as shown in Figure 15. We had three setups in these two environments for the results reported in this article. The first setup was within the *laboratory*, in a 4.5×8.8 m^2 room. The room was crowded with tables and PCs, which blocked part of the LOS paths and formed a complex radio propagation environment. The second setup was a *through-wall* scenario, where the person was on the transmitter side, separated by a wall (and a metal door) from the receiver. The third setup was a 20×2.2 m^2 *long corridor*, where the receiver and the transmitter were 11 m apart. We used omnidirectional antennas at both the receiver and transmitter for breathing rate estimation in all three scenarios. We used a directional antenna at the transmitter in the laboratory scenario for heart rate estimation. For comparison purposed, we employed the NEULOG Respiration Monitor Belt Logger Sensor and a fingertip pulse oximeter to record the ground truths of the breathing and heart rates.

4.2 Performance of Breathing and Heart Rate Estimation

Figure 16 presents the cumulative distribution functions (CDFs) of estimation error in breathing rate estimation. We use the CSI amplitude-based method [Liu et al. 2015] as a benchmark in this experiment. We can see that both systems have a similar median estimate error of 0.25 bpm. However, for PhaseBeat, 90% of the tests have an estimated error under 0.5 bpm, whereas for the amplitude-based method, 70% of the tests have an estimated error under 0.5 bpm. Moreover, the maximum estimation error for PhaseBeat and the amplitude-based method are 0.85 and 1.7 bpm, respectively. This is because amplitude is more sensitive to the influence of RSS. When the received signal is greatly weakened by the long distance or the multipath effect, the CSI amplitude can hardly reflect the small movements of the human chest and heartbeats. In contrast, since the CSI phase is not related to
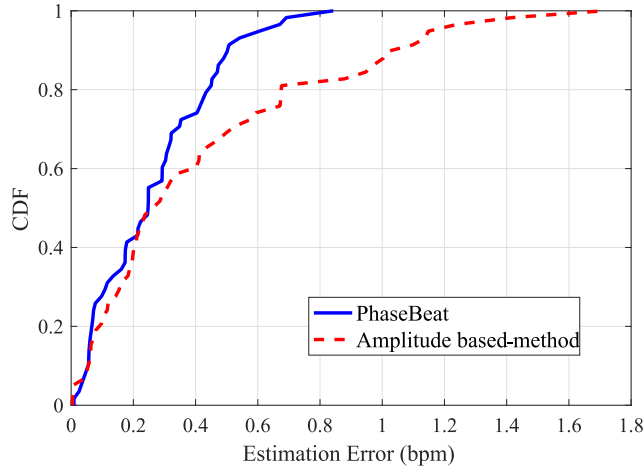
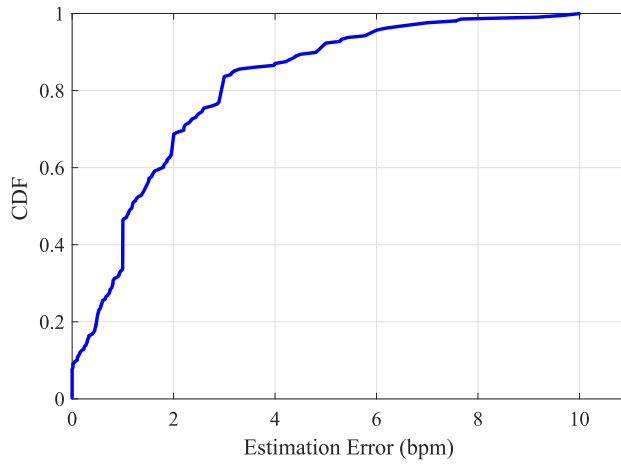Fig. 16. CDFs of estimation errors of breathing rate estimation.

Fig. 17. CDFs of estimation errors of heart rate estimation.

the RSS, the influence of signal strength (and hence multipath) on phase information is limited. Therefore, our PhaseBeat system achieves considerably higher accuracy than the amplitude-based method for breathing rate estimation.

Figure 17 presents the CDF of estimation error of heart rate estimation. For heart signal monitoring, we use a directional antenna at the transmitter to improve the strength of the chest-reflected signal. In Figure 17, we find that PhaseBeat has a median estimate error of 1.19 bpm, whereas 80% of the test data has an estimated error under 2.91 bpm. Moreover, the maximum estimation error for PhaseBeat is 10.02 bpm. We notice that the estimation accuracy of heart rate is lower than that of breathing rate estimation because of the much weaker heart signal.

Figure 18 shows the accuracy of breathing and heart rate estimation for different sampling frequencies. For data calibration, we adopt a 400-Hz sampling frequency to estimate the vital signs, which is sufficient to accurately detect both vital sign signals. As shown in the figure, the breathing rate estimation has a similar low
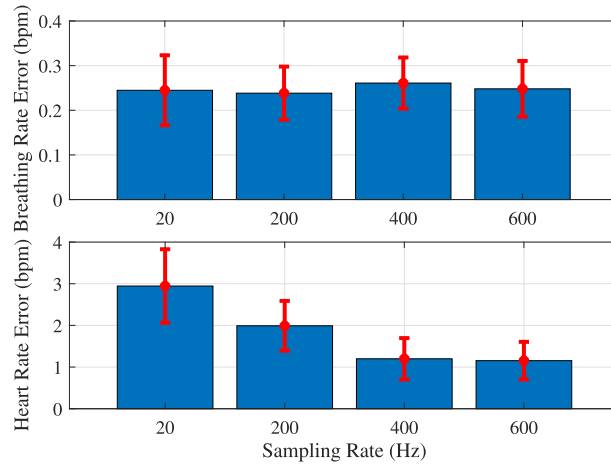
Fig. 18. Estimation errors of breathing and heart rate estimation at different sampling frequency.
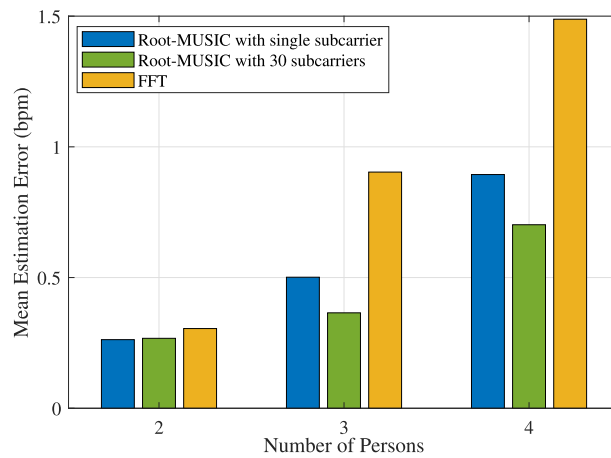

Fig. 19. Mean estimation errors of breathing rates for different numbers of persons.

estimation error of 0.25 bpm for different sampling frequencies. However, the median error of heart rate estimation is 2.91 bpm when the sampling rate is 20-Hz, and 1.19 bpm when the sampling rate is 400-Hz. Thus, we chose the 400-Hz sampling rate for PhaseBeat, which is used for all other experimental results in this article.

Figure 19 shows the accuracy of breathing rate estimation for different numbers of persons. Moreover, we compare the proposed root-MUSIC-based method using 30 subcarriers with the FFT-based method, and with root-MUSIC method using a single subcarrier. It is noticed that for multiple persons, the accuracy of breathing rate estimation degrades for all three schemes. We can see that for two-person breathing rate estimation, the three methods all have a very low estimation error that is lower than 0.29 bpm. However, in the case of four persons, the mean estimation errors are 0.89, 0.70, and 1.48 bpm for root-MUSIC with 30 subcarriers, root-MUSIC with a single subcarrier, and FFT, respectively. The root-MUSIC-based method using 30 subcarriers achieves the best performance among the three schemes in all cases. For scenarios with more than four persons, even root-MUSIC
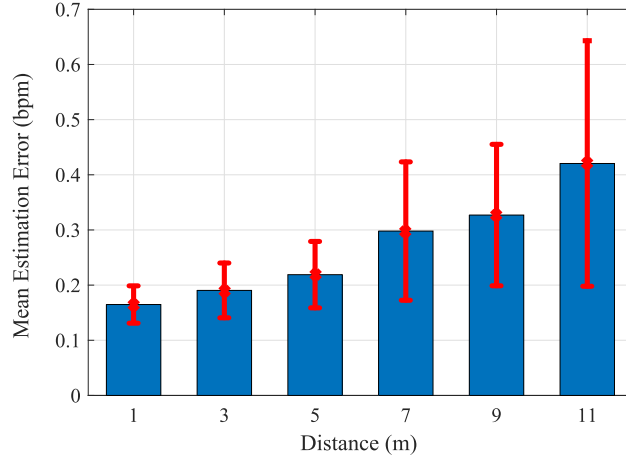
Fig. 20. Impact of the distance between the transmitter and the receiver in the long corridor case.
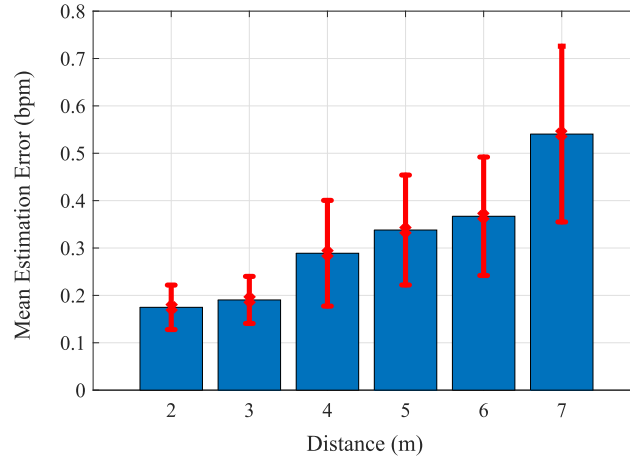

Fig. 21. Impact of the distance between the transmitter and the receiver in the through-wall scenario.

cannot achieve a sufficiently accurate estimation for breath monitoring. Thus, we find that the maximum number of persons for the system is 4.

4.3 Impact of Various Factors

4.3.1 Impact of the Transmitter-Receiver Distance. Figure 20 and Figure 21 show the impact of the distance between the transmitter and the receiver for the long corridor and through-wall scenarios, respectively. When the transmitter-receiver distance is increased, the mean estimation error also increases. This is because the reflected signal is reduced when the distance between the transmitter and receiver is long, which influences the dynamic range of phase difference data. Moreover, we find that the mean estimation error at the same distance for the through-wall scenario is larger than that for the long corridor scenario. For example, when the distance is 7 m, the mean estimation errors for the long corridor and the through-wall scenario are 0.30 and 0.52 bpm, respectively. This is because the signal in the through-wall scenario experiences a much larger attenuation than that in the long corridor scenario.
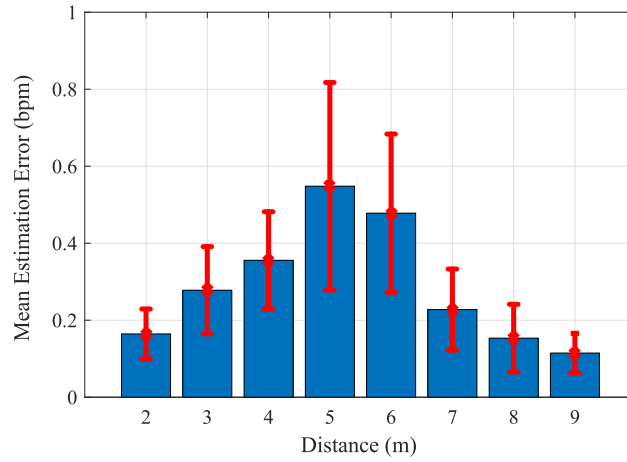
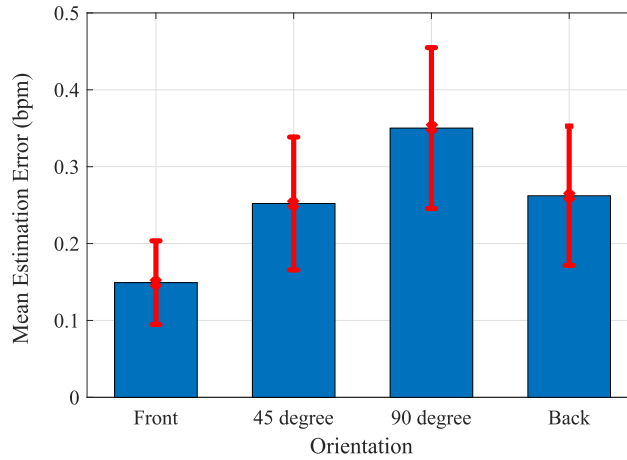Fig. 22. Impact of the distance between the user and the receiver.

Fig. 23. Impact of user orientation relative to the receiver on breathing estimation.

4.3.2 Impact of the User-Receiver Distance. Figure 22 shows the impact of the distance between the user and the receiver in the long corridor scenario. We find that when the user is located in the middle of the transmitter and receiver, the mean estimation error is the maximum at 0.52 bpm. In addition, when the user is close to either the transmitter or the receiver, the estimation error assumes the minimum values at 0.11 and 0.15 bpm, respectively. When the user is far away with the WiFi devices, the reflected signal from the transmitter is greatly weakened, which influences the usefulness of the collected phase difference data.

4.3.3 Impact of User Orientation Relative to the Receiver. Figure 23 shows the impact of user orientation with respect to the receiver in the laboratory environment. We consider four cases, including front (0°), 45°, 90°, and back (180°). As shown in Figure 18, the mean estimation error achieves the maximum at 0.35 bpm at the 90° direction, whereas the minimum error of 0.14 bpm is achieved at the front orientation. When the user orientation relative to the receiver is front or back, the reflected component of the wireless signal can effectively capture the chest movements (i.e., inhaling or exhaling). Thus, we can achieve relatively lower estimation errors in these cases.
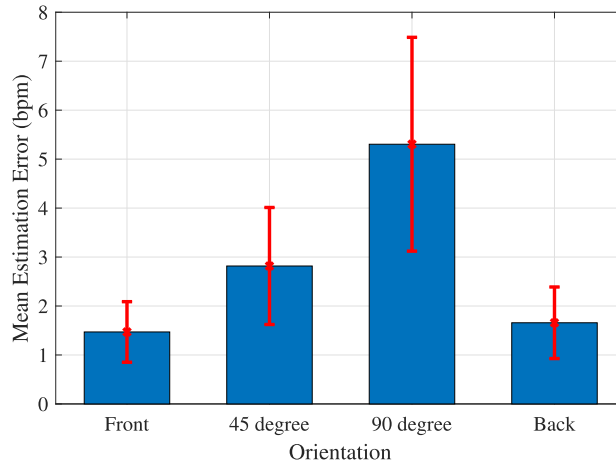
Fig. 24. Impact of user orientation relative to the receiver on heart rate estimation.
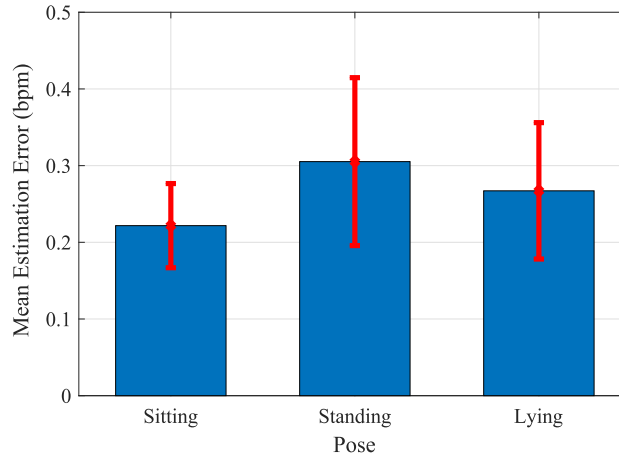

Fig. 25. Impact of different poses of the user.

Figure 24 shows the impact on heart rate estimation of user orientation relative to the receiver in the laboratory environment. We consider the same four cases including front (0°), 45°, 90°, and back (180°). As shown in the figure, the mean estimation error is the maximum at 5.30 bpm at the 90° direction, whereas the minimum error of 1.41 bpm is achieved at the front orientation. When the user orientation is front or back, the wireless signal can penetrate the human chest more easily and capture the heart movements more accurately. Thus, we can achieve relatively lower estimation errors in these cases.

4.3.4 Impact of the User Pose. Figure 25 shows the impact of different user poses on respiration rate estimation in the laboratory scenario. We consider three common poses of a stationary person, including sitting, standing, and lying. As shown in Figure 25, for the standing pose, the mean estimation error is 0.31 bpm, which is larger than the other two poses: sitting with a 0.22-bpm mean error and lying with a 0.26-bpm mean error. This is because the chest of the person will have weaker reflection of the WiFi signal when the person is standing.
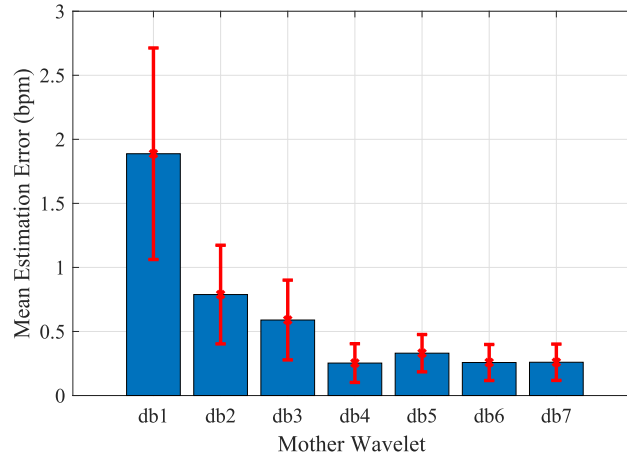
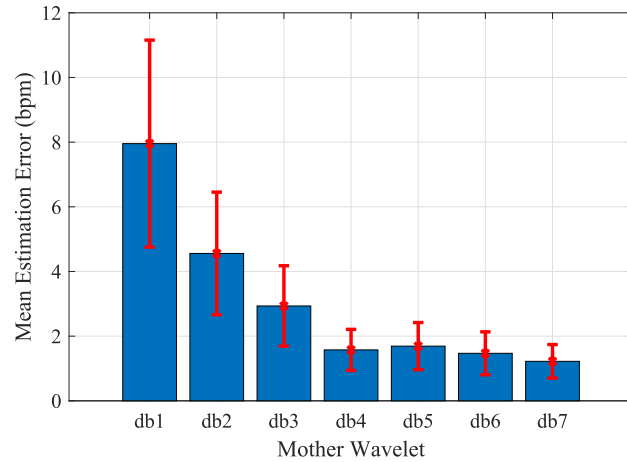Fig. 26. Impact of different mother wavelets on breathing estimation.

Fig. 27. Impact of different mother wavelets on heart rate estimation.

4.3.5 Impact of Different Mother Wavelets. Figure 26 shows the impact of different Daubechies mother wavelets on breathing rate estimation. We find that the db1 mother wavelet achieves a 1.82-bpm mean error for breathing rate estimation, which means that this mother wavelet may not be suitable for breathing signal analysis. However, decompositions based on the db2-db7 mother wavelets all achieve a mean error lower than 1 bpm, which means that these mother wavelets are sufficient for breathing rate analysis. Even though the db2 and db3 mother wavelets cannot obtain a very smooth waveform, the denoising signal has already had exacted peaks for peak detection function. The db4-db7 mother wavelets all achieve very high accuracy for breathing rate estimation.

Figure 27 presents the impact of different mother wavelets on heart rate estimation. We can see that when the db1 mother wavelet is used for DWT, the mean error is 7.95 bpm. Thus, db1 is not effective in analyzing the heartbeat signal. The reason is that the decomposition based on the db1 mother wavelet has poor denoising performance. The obtained heartbeat signal looks more like a square wave, making it hard to estimate heart rate using FFT. When we use higher db mother wavelets to decompose the signal, the denoising effect becomes more

effective and the estimation becomes more accurate. As the db2 and db3 mother wavelets are used, the denoising effect becomes much better, but there are still some small peaks in the remaining signal. When the db4 mother wavelet is used, there are no longer any ripples in the recovered heartbeat signals. The mean error becomes 1.51 bpm. The db5, db6, and db7 mother wavelets all achieve a similar estimation error. Therefore, we use the db4 mother wavelet to decompose the original signal in PhaseBeat.

5 RELATED WORK

This work is closely related to two categories of vital sign monitoring: sensor-based and RF signal–based systems, which are reviewed in the following.

Sensor-based systems for vital sign monitoring leverage special hardware attached to the human body. Typically, special devices, such as a capnometer that can measure carbon dioxide (CO2) concentrations in respired gases, are used to monitor patients' breathing rate in hospitals [Mogue and Rantala 1988]. However, it is uncomfortable to wear and is mainly used in clinical environments. Photoplethysmography (PPG) is an optical technique to measure the blood volume variations in the tissues by detecting the changes in light absorption by attaching the sensor to the patient's finger (e.g., pulse oximeters) [Shariati and Zahedi 2005]. Moreover, a smartphone can utilize the embedded camera to measure light changes. The pixel of the captured video frame is transformed into RGB components, which can detect the PPG signal to estimate the heart rate [Scully et al. 2010]. Recently, smartphones have been used to measure the breathing rate using the built-in accelerometer, gyroscope [Aly and Youssef 2016], and microphone [Ren et al. 2015; Wang et al. 2017a, 2017b], which require the user to place the smartphone near the body or wear some sensors. These techniques all require sensors attached to the patient's body, which cannot be applied for remote (or unobtrusive) monitoring of vital signs.

RF-based systems for vital sign monitoring exploit RF signals to extract the breathing-induced chest movements, which is mainly based on radar and WiFi techniques. For radar-based vital sign monitoring, techniques such as Doppler radar [Droitcour et al. 2009; Nguyen et al. 2016] and ultra-wideband radar [Salmi and Molisch 2011] were developed, which require special hardware operating at a wide spectrum. A recent work employed an FMCW radar to estimate breathing and heart rates, even for multiple subjects [Adib et al. 2015]. However, this system also required customized hardware and a large bandwidth from 5.46 to 7.25 GHz to operate.

To reduce cost, some RFID-based systems have been developed [Hou et al. 2017; Yang et al. 2018a, 2019]. In these RFID systems, the breathing signals can be extracted from the backscattered signals from the passive RFID tags attached to the patient's clothes. Although these systems can achieve both high accuracy and lower cost over radar-based systems, the user has to stay close to the RFID reader due to the short scanning range of the reader.

Different from RFID-based techniques, WiFi-based systems can monitor human vital signs in a larger area, and the cost of the system is low. Today, WiFi has been widely employed for indoor localization [Chen et al. 2017; Du et al. 2018] and human activity detection [Gu et al. 2017; Xu et al. 2019; Yang et al. 2018b], as well as monitoring human vital signs and body movements [Fan et al. 2016]. Among these techniques, BodyScan is an independent wearable system that can detect both human vital signs and recognize human activities accurately. Since the users are required to equip the special device on the body, the system may not suitable for long-term sensing, especially when the user is sleeping. WiFi RSS is leveraged in UbiBreathe to estimate human respiration, which requires the patient to stay in the LOS path between the WiFi transmitter and the receiver [Abdelnasser et al. 2015]. The mmVital system uses the RSS of 60-GHz millimeter wave (mmWave) signals for breathing and heart rate estimation [Yang et al. 2016]. This technique does not work over a relatively longer distance and requires a high gain directional antenna at both the transmitter and the receiver. Recently, Liu et al. [2015] exploited CSI amplitude of WiFi to track vital signs. This work is focused on monitoring breathing and heart rates of one sleeping person, whereas another work leveraged CSI phase to measure the human respiration signal [Zhang et al. 2019].

Our system is motivated by these interesting prior works. To the best of our knowledge, this is the first to leverage CSI phase difference data to remotely detect breathing and heart rates with commodity WiFi devices [Wang et al. 2017d]. It can achieve a higher estimation accuracy of vital signs including both breathing and heart rates, with easy, low-cost deployment. This work also provides a rigorous analysis of the CSI phase data, which proves the feasibility of exploiting CSI phase difference for vital sign monitoring.

6 CONCLUSION

In this article, we presented PhaseBeat to exploit CSI phase difference data to monitor breathing and heartbeats with commodity WiFi devices. We first provided a rigorous analysis of CSI phase difference data with respect to its stability and periodicity. We then described the PhaseBeat design in detail, including environment detection, data calibration, subcarrier selection, and DWT. We implemented PhaseBeat with off-the-shelf WiFi devices and conducted an extensive experimental study with three scenarios. The experimental results showed that PhaseBeat could achieve superior performance on breathing and heart rate detection over existing methods.

REFERENCES

H. Abdelnasser, K. A. Harras, and M. Youssef. 2015. UbiBreathe: A ubiquitous non-invasive WiFi-based breathing estimator. In *Proceedings of IEEE MobiHoc 2015*. 277–286.

F. Adib, H. Mao, Z. Kabelac, D. Katabi, and R. Miller. 2015. Smart homes that monitor breathing and heart rate. In *Proceedings of ACM CHI 2015*. 837–846.

H. Aly and M. Youssef. 2016. Zephyr: Ubiquitous accurate multi-sensor fusion-based respiratory rate estimation using smartphones. In *Proceedings of IEEE INFOCOM 2016*. 1–9.

O. Boric-Lubecke and V. M. Lubecke. 2002. Wireless house calls: Using communications technology for health care and monitoring. *IEEE Microwave Magazine* 3, 3 (2002), 43–48.

Chen Chen, Yan Chen, Yi Han, Hung-Quoc Lai, and K. J. Ray Liu. 2017. Achieving centimeter-accuracy indoor localization on WiFi platforms: A frequency hopping approach. *IEEE Internet of Things Journal* 4, 1 (Feb. 2017), 111–121.

A. Droitcour, O. Boric-Lubecke, and G. Kovacs. 2009. Signal-to-noise ratio in Doppler radar system for heart and respiratory rate measurements. *IEEE Transactions on Microwave Theory and Techniques* 57, 10 (Oct. 2009), 2498–2507.

Xuan Du, Kun Yang, and Dongdai Zhou. 2018. MapSense: Mitigating inconsistent WiFi signals using signal patterns and pathway map for indoor positioning. *IEEE Internet of Things Journal* 5, 6 (Dec. 2018), 4652–4662.

Biyi Fang, Nicholas D. Lane, Mi Zhang, Aidan Boran, and Fahim Kawsar. 2016. *BodyScan*: Enabling radio-based sensing on wearable devices for contactless activity and vital sign monitoring. In *Proceedings of ACM MobiSys 2016*. 97–110.

J. Gjengset, J. Xiong, G. McPhillips, and K. Jamieson. 2014. Phaser: Enabling phased array signal processing on commodity WiFi access points. In *Proceedings of ACM MobiCom 2014*. 153–164.

Yu Gu, Jinhai Zhan, Yusheng Ji, Jie Li, Fuji Ren, and Shangbing Gao. 2017. MoSense: An RF-based motion detection system via off-the-shelf WiFi devices. *IEEE Internet of Things Journal* 4, 6 (Dec. 2017), 2326–2341.

D. Halperin, W. J. Hu, A. Sheth, and D. Wetherall. 2010. Predictable 802.11 packet delivery from wireless channel measurements. In *Proceedings of ACM SIGCOMM 2010*. 159–170.

Yuxiao Hou, Yanwen Wang, and Yuanqing Zheng. 2017. TagBreathe: Monitor breathing with commodity rfid systems. In *Proceedings of IEEE ICDCS 2017*. IEEE, Los Alamitos, CA, 404–413.

C. Hunt and F. Hauck. 2006. Sudden infant death syndrome. *Canadian Medical Association Journal* 174, 13 (2006), 1309–1310.

Zhenhua Jia, Musaab Alaziz, Xiang Chi, Richard E. Howard, Yanyong Zhang, Pei Zhang, Wade Trappe, Anand Sivasubramaniam, and Ning An. 2016. HB-Phone: A bed-mounted geophone-based heartbeat monitoring system. In *Proceedings ACM/IEEE IPSN 2016*. 1–12.

Zhenhua Jia, Amelie Bonde, Sugang Li, Chenren Xu, Jingxian Wang, Yanyong Zhang, Richard E. Howard, and Pei Zhang. 2017. Monitoring a person's heart rate and respiratory rate on a shared bed using geophones. In *Proceedings of ACM SenSys 2017*. 1–14.

J. Liu, Y. Wang, Y. Chen, J. Yang, X. Chen, and J. Cheng. 2015. Tracking vital signs during sleep leveraging off-the-shelf WiFi. In *Proceedings of ACM MobiHoc 2015*. 267–276.

S. Mao, X. Wang, and L. Gao. 2016. BiLoc: Bi-modal deep learning for indoor localization with commodity 5GHz WiFi. US Provisional Patent Application, Application Number: 62/338,737.

M. L. R. Mogue and B. Rantala. 1988. Capnometers. *Journal of Clinical Monitoring* 4, 2 (1988), 115–121.

Rajalakshmi Nandakumar, Shyamnath Gollakota, and Jacob E. Sunshine. 2019. Opioid overdose detection using smartphones. *Science Translational Medicine* 11, 474 (2019), 1–10.

Rajalakshmi Nandakumar, Shyamnath Gollakota, and Nathaniel Watson. 2015. Contactless sleep apnea detection on smartphones. In *Proceedings of ACM MobiSys 2015*. 45–57.

Phuc Nguyen, Xinyu Zhang, Ann Halbower, and Tam Vu. 2016. Continuous and fine-grained breathing volume monitoring from afar using wireless signals. In *Proceedings of IEEE INFOCOM 2016*.

Kun Qian, Chenshu Wu, Zheng Yang, Yunhao Liu, and Zimu Zhou. 2014. PADS: Passive detection of moving targets with dynamic speed using PHY layer information. In *Proceedings of IEEE ICPADS 2014*. 1–8.

B. D. Rao and K. V. S. Hari. 1989. Performance analysis of root-music. *IEEE Transactions on Acoustics Speech and Signal Processing* 37, 12 (Dec. 1989), 1939–1949.

Y. Ren, C. Wang, J. Yang, and Y. Chen. 2015. Fine-grained sleep monitoring: Hearing your breathing with smartphones. In *Proceedings of IEEE INFOCOM 2015*. 1194–1202.

J. Salmi and A. F. Molisch. 2011. Propagation parameter estimation, modeling and measurements for ultrawideband MIMO radar. *IEEE Transactions on Antennas and Propagation* 59, 11 (Nov. 2011), 4257–4267.

S. Sardy, P. Tseng, and A. Brace. 2001. Robust wavelet denoising. *IEEE Transactions on Signal Processing* 49, 6 (Jun. 2001), 1146–1152.

C. G. Scully, J. Lee, J. Meyer, A. M. Gorbach, D. Granquist-Fraser, Y. Mendelson, and K. H. Chon. 2010. Physiological parameter monitoring from optical recordings with a mobile phone. *IEEE Transactions on Biomedical Engineering* 59, 2 (Feb. 2010), 303–306.

N. H. Shariati and E. Zahedi. 2005. Comparison of selected parametric models for analysis of the photoplethysmographic signal. In *Proceedings of the 1st IEEE International Conference on Computers, Communications, and Signal Processing with Special Track on Biomedical Engineering*. 169–172.

M. Speth, S. Fechtel, G. Fock, and H. Meyr. 1999. Optimum receiver design for wireless broad-band systems using OFDM–Part I. *IEEE Transactions on Communications* 47, 11 (Nov. 1999), 1668–1677.

X. Wang, L. Gao, and S. Mao. 2015. PhaseFi: Phase fingerprinting for indoor localization with a deep learning approach. In *Proceedings of IEEE GLOBECOM 2015*. 1–6.

X. Wang, L. Gao, and S. Mao. 2016. CSI phase fingerprinting for indoor localization with a deep learning approach. *IEEE Internet of Things Journal* 3, 6 (Dec. 2016), 1113–1123. DOI : https://doi.org/10.1109/JIOT.2016.2558659

X. Wang, R. Huang, and S. Mao. 2017a. Demo abstract: SonarBeat: Sonar phase for breathing beat monitoring with smartphones. In *Proceedings of IEEE SECON 2017*. 1–2.

X. Wang, R. Huang, and S. Mao. 2017b. SonarBeat: Sonar phase for breathing beat monitoring with smartphones. In *Proceedings of ICCCN 2017*. 1–8.

X. Wang, X. Wang, and S. Mao. 2017c. CiFi: Deep convolutional neural networks for indoor localization with 5GHz Wi-Fi. In *Proceedings of IEEE ICC 2017*. 1–6.

X. Wang, C. Yang, and S. Mao. 2017d. PhaseBeat: Exploiting CSI phase data for vital sign monitoring with commodity WiFi devices. In *Proceedings of IEEE ICDCS 2017*. 1230–1239.

X. Wang, C. Yang, and S. Mao. 2017e. TensorBeat: Tensor decomposition for monitoring multi-person breathing beats with commodity WiFi. *ACM Transactions on Intelligent Systems and Technology* 9, 1 (Sept. 2017), Article 8, 27 pages. DOI : https://doi.org/10.1145/3078855

Chenshu Wu, Zheng Yang, Zimu Zhou, Kun Qian, Yunhao Liu, and Mingyan Liu. 2015. PhaseU: Real-time LOS identification with WiFi. In *Proceedings of IEEE INFOCOM 2015*. 2038–2046.

Y. Xie, Z. Li, and M. Li. 2015. Precise power delay profiling with commodity WiFi. In *Proceedings of ACM MobiCom 2015*. 53–64.

J. Xiong and K. Jamieson. 2013. ArrayTrack: A fine-grained indoor location system. In *Proceedings of ACM NSDI 2013*. 71–84.

Qinyi Xu, Yi Han, Beibei Wang, Min Wu, and K. J. Ray Liu. 2019. Indoor events monitoring using channel state information time series. *IEEE Internet of Things Journal* 6, 3 (June 2019), 4977–4990.

C. Yang, X. Wang, and S. Mao. 2018a. AutoTag: Recurrent vibrational autoencoder for unsupervised apnea detection with RFID tags. In *Proceedings of IEEE GLOBECOM 2018*. 1–6.

C. Yang, X. Wang, and S. Mao. 2019. RFID-based driving fatigue detection. In *Proceedings of IEEE GLOBECOM 2019*. 1–6.

Jianfei Yang, Han Zou, Hao Jiang, and Lihua Xie. 2018b. Device-free occupant activity sensing using WiFi-enabled IoT devices for smart homes. *IEEE Internet of Things Journal* 5, 5 (Oct. 2018), 3991–4002.

Z. Yang, P. Pathak, Y. Zeng, X. Liran, and P. Mohapatra. 2016. Monitoring vital signs using millimeter wave. In *Proceedings of IEEE MobiHoc 2016*.

Z. Yang, Z. Zhou, and Y. Liu. 2013. From RSSI to CSI: Indoor localization via channel response. *ACM Computing Surveys* 46, 2 (Nov. 2013), Article 25.

Dongheng Zhang, Yang Hu, Yan Chen, and Bing Zeng. 2019. BreathTrack: Tracking indoor human breath status via commodity WiFi. *IEEE Internet of Things Journal* 6, 2 (April 2019), 3899–3911.